Applied Physics Letters

Assessing the impact of disjoining pressure on thin-film evaporation with atomistic simulation and kinetic theory

Cite as: Appl. Phys. Lett. **116**, 213701 (2020); https://doi.org/10.1063/5.0010467
Submitted: 17 April 2020 . Accepted: 13 May 2020 . Published Online: 27 May 2020

Xiaoman Wang, Yang Li, Jonathan A. Malen, and Alan J. H. McGaughey

Applied Physics Letters ARTICLE scitation.org/journal/apl

Assessing the impact of disjoining pressure on thin-film evaporation with atomistic simulation and kinetic theory

Cite as: Appl. Phys. Lett. **116**, 213701 (2020); doi: 10.1063/5.0010467
Submitted: 17 April 2020 · Accepted: 13 May 2020 ·
Published Online: 27 May 2020

Xiaoman Wang, Yang Li, Jonathan A. Malen, and Alan J. H. McGaughey[a)]

AFFILIATIONS

Department of Mechanical Engineering, Carnegie Mellon University, Pittsburgh, Pennsylvania 15213, USA

[a)]Author to whom correspondence should be addressed: mcgaughey@cmu.edu

ABSTRACT

Molecular dynamics (MD) simulations are applied to validate the Hertz–Knudsen–Schrage (HKS) relation for the evaporation mass flux in the presence of disjoining pressure. A non-equilibrium MD simulation system is designed to directly extract the evaporation mass flux for a Lennard-Jones fluid. The temperatures, pressures, properties, and disjoining pressure required to evaluate the HKS relation are obtained from the non-equilibrium MD simulation and complementary equilibrium MD simulations. The direct MD evaporation mass flux and that from the HKS relation agree within 10%. We define an evaporation Kapitza length that estimates where the liquid conduction and evaporation thermal resistances are equal. We propose that surface structures that promote film thicknesses comparable to or smaller than the evaporation Kapitza length, but larger than the adsorbed film thickness, will maximize the evaporation rate.

Increasing power densities in microelectronics pose challenges in the design of thermal management strategies for achieving desirable operating temperatures.[1,2] Evaporative cooling is a promising option because the large latent heat of vaporization leads to heat transfer coefficients that are several orders of magnitude greater than those for forced and free convection.[3,4] Evaporation from the nanometer-thick liquid region of a meniscus is particularly attractive. The dimensions of microstructured surfaces can be carefully designed to enlarge this region so as to maximize the evaporation mass flux in heat pipes and thermosyphons.[5–7] Meniscus evaporation is also critical for seawater desalination and solar thermal generators;[8,9] lubrication;[10,11] heating, ventilation, and air conditioning systems;[12,13] and medical devices.[14,15]

The evaporation rate from a meniscus is controlled by a competition between a high superheat at the liquid–vapor interface and a suppressed liquid pressure due to the effects of the capillary pressure (P_c) and/or the disjoining pressure (P_d). P_c depends on the meniscus curvature and decreases as the meniscus becomes flatter. P_d was first proposed by Derjaguin *et al.*[16] to capture the long-range intermolecular forces between a liquid film and its solid substrate. P_d decreases rapidly with increasing film thickness. The variations of P_d and P_c in the meniscus lead to a gradient in the liquid pressure, which drives the liquid flow needed to maintain the evaporation.[17] These pressure variations also influence the atomic kinetics at the liquid–vapor interface. Thus, P_d and P_c separate the meniscus into three regions, as shown in Fig. 1: (i) the non-evaporating adsorbed film, where a thin liquid film results from a strong P_d that fully suppresses evaporation, (ii) the evaporating thin film, where the highest local evaporation mass flux ($\dot{m}''_{evap}$) is reached because of the small liquid conduction resistance (R_{cond}) and a small P_d,[18–21] and (iii) the bulk film region, where evaporation is limited by the high liquid conduction resistance. The variations of P_d, P_c, $\dot{m}''_{evap}$, and R_{cond} in the three regions are shown in Fig. 1. Our focus is on regions (i) and (ii), where P_c is normally far smaller than P_d.[22] We note that P_c can be comparable to P_d in region (ii) in a nanochannel.[23]

Over the past century, efforts have been devoted to mathematically describing the evaporation process. The widely used Hertz–Knudsen (HK) relation assumes an equilibrium Maxwell–Boltzmann velocity distribution at the liquid–vapor interface.[24] In 1953, Schrage modified the HK relation by hypothesizing that the velocity distribution at the liquid-vapor interface shifts away from the Maxwell-Boltzmann distribution by the macroscopic vapor velocity.[25] The resulting Hertz–Knudsen–Schrage (HKS) relation is

$$\dot{m}''_{evap} = \alpha(T_{lv})\sqrt{\frac{m}{2\pi k_B}}\left[\frac{P_{eq}(T_{lv})}{\sqrt{T_{lv}}} - \Gamma(v_R)\frac{P_v}{\sqrt{T_v}}\right], \tag{1}$$

where the subscripts refer to the liquid (l) and vapor (v) phases, α is the mass accommodation coefficient at the liquid–vapor interface, T_{lv} is the liquid–vapor interface temperature, k_B is the Boltzmann

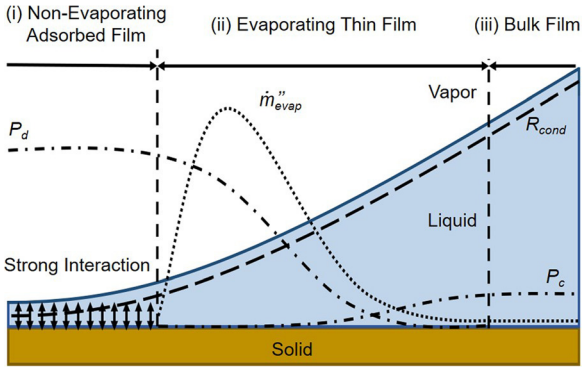

FIG. 1. Schematic drawing of the three regions in the meniscus. The focus of this study is evaporation in regions (i) and (ii).

constant, m is the atomic mass, P_v is the vapor pressure, T_v is the vapor temperature, P_{eq} is the equilibrium pressure, and $\Gamma(v_R)$ accounts for the shifted velocity distribution. Further details on P_{eq} and $\Gamma(v_R)$ are provided later.

Experimental validation of the HK and HKS relations is challenging. The interface temperature T_{lv} cannot be directly measured and must be inferred from nearby temperature gradients and fluid properties.[26–28] Moreover, the uncertainty associated with specifying α, which represents the probability for a vapor molecule to strike the interface and be absorbed by the liquid, is large. For water alone, the reported α values vary from 10^{-4} to 1.[29]

Molecular dynamics (MD) simulations, which track atomic trajectories, provide an approach to test these theories. Liang *et al.* recently validated the HKS relation using MD simulations of a thick, flat liquid–vapor interface (i.e., $P_d = P_c = 0$) of a Lennard-Jones (LJ) fluid.[30] Their predictions agree with $\dot{m}''_{evap}$ values directly observed in their MD simulations to within 10% for a range of conditions. The accuracy of the HKS relation in the presence of P_d, however, has not been assessed. Wang *et al.* studied the influence of P_d on the evaporation of an LJ thin liquid film, but only compared the observed $\dot{m}''_{evap}$ with the HKS relation when P_d was insignificant.[31] Han calculated the evaporation rate with P_d for an LJ liquid, but only compared it with the HK relation with $\alpha = 1$.[32] He found that using classic Hamaker theory to describe P_d cannot predict $\dot{m}''_{evap}$ in the thin film region.

The objective of this study is to apply MD simulations to determine if the HKS relation, Eq. (1), is valid when P_d is important. A flat liquid–vapor interface is studied so that the influence of P_c can be ignored. The LJ fluid is chosen because its liquid/vapor density ratio is small compared to fluids like water, which enables good statistics for the vapor properties. Moreover, the LJ fluid was used in previous validation studies.[30,31,33,34] We find that including P_d is essential for predicting the evaporation rate in the evaporating thin film [region (ii) in Fig. 1] and quantify how the liquid conduction and evaporation thermal resistances change as a function of film thickness.

To test the validity of the HKS relation in the presence of P_d, we built a non-equilibrium MD (NEMD) simulation with a temperature difference across the system, as shown in Fig. 2. The system consists of an LJ argon fluid confined by two LJ solid plates with the same mass and length scale as the fluid but an energy scale ten times larger. The Lorentz–Berthelot mixing rules[35,36] are used for the interactions between fluid and solid atoms. The dimensions of the simulation box are provided in Fig. 2. Periodic boundary conditions are applied in the x and y directions. In the z direction, two layers of atoms at each end serve as fixed boundaries. The MD simulations are run using LAMMPS[37] with a time step of 5 fs. The fluid is obtained by melting a crystal by raising the system temperature at a rate of 1.6 K/ns from 5 to 85 K. Afterwards, the system is equilibrated at a temperature of 85 K for 50 ns. The hot and cold reservoirs are then set to temperatures of 100 and 70 K so as to initiate evaporation and condensation. More details about the simulations are provided in Sec. S1.

The simulated $\dot{m}''_{evap}$ is directly obtained as the time rate of change of the number of liquid atoms left on the evaporation side using a central difference formula. Liquid atoms are defined as those fluid atoms that have at least four neighboring atoms within 1.5σ (Sec. S3C).[38–40] Eight independent simulations were run (Sec. S1). The mass flux data from all eight simulations were sorted based on the film thickness into bins of width 1 Å and then averaged.

The theoretical $\dot{m}''_{evap}$ is predicted by extracting the necessary properties from the MD simulation and using them as inputs to the HKS relation, Eq. (1). Faghri derived an expression for the equilibrium pressure,[41]

$$P_{eq}(T_{lv}) = P_{sat}(T_{lv}) \times \exp\left[\frac{P_{eq}(T_{lv}) - P_{sat}(T_{lv}) - P_d(L) - P_c}{\rho_l T_{lv} k_B / m}\right], \tag{2}$$

where $P_{sat}(T_{lv})$ is the saturation pressure at T_{lv} when P_c and P_d are negligible, ρ_l is the density of the liquid film, and L is the film thickness. Schrage proposed the form of $\Gamma(v_R)$, which is a function of the shifted velocity distribution, to be

$$\Gamma(v_R) = \exp(-v_R^2) - v_R\sqrt{\pi}[1 - \mathrm{erf}(v_R)]. \tag{3}$$

Here, the dimensionless velocity v_R is given by

$$v_R = \frac{v_0}{\sqrt{2k_B T_v/m}}, \tag{4}$$

where v_0 is the macroscopic vapor speed and $\sqrt{2k_B T_v/m}$ is the most probable speed of the vapor atoms based on the Maxwell–Boltzmann distribution.[30] Since v_0 is determined by $\dot{m}''_{evap}$, the mass flux predicted from Eq. (1) needs to be calculated numerically.

To determine if our NEMD simulation system satisfies the ideal gas law assumption underlying Eqs. (1)–(4), we compared P_v with the vapor pressure calculated using the ideal gas law $P_{ideal} = \rho_v R T_v$. The compressibility factor P_v/P_{ideal} has an average value of 0.93 over the NEMD simulation, indicating that the ideal gas law assumption is acceptable.[42–44]

The instantaneous time-dependent properties T_{lv}, T_v, and P_v in Eqs. (1)–(4) can be directly obtained from the NEMD simulation. The properties $\alpha(T_{lv})$, $P_{sat}(T_{lv})$, and $P_d(L)$, however, need to be calculated using separate equilibrium MD (EMD) simulations based on the corresponding liquid-vapor interface temperature and/or the film thickness of the NEMD system at each time step. To do so, we built two EMD systems: (i) a system without a solid component for extracting the temperature-dependent properties α and P_{sat} (Sec. S2) and (ii) a system with a single solid component for extracting the film thickness-dependent P_d (Sec. S3). The resulting α, P_{sat}, and P_d are fit to empirical relations, which are then used in evaluating Eq. (1).

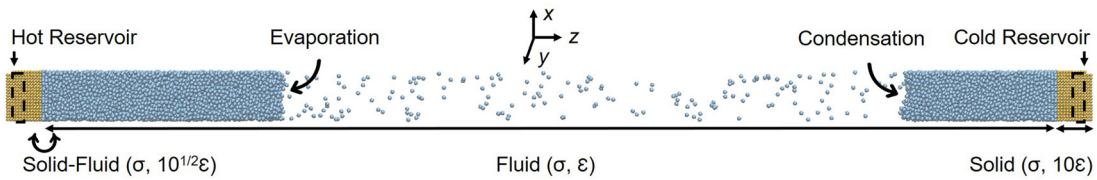

FIG. 2. NEMD system setup. The cross-sectional area is $4.25 \times 4.25\,\text{nm}^2$, and the total length is 100.99 nm. There are 3072 solid atoms and 12 800 fluid atoms. A 12–6 LJ potential is used with $\sigma = 3.4$ Å and $\varepsilon = 1.67 \times 10^{-21}$ J.

The liquid–vapor interface needs to be located to calculate the film thickness. Previous studies defined the interface as the center of the transition region in the density profile (i.e., the region where the density changes from 90% to 10% of the liquid density[45,46]) With ultra-thin films, however, it can be challenging to obtain the density profile. Inspired by ten Wolde and Frenkel,[47] we use the number of neighbor atoms to determine if an atom is at the liquid–vapor interface. If an atom has two or three neighbors within 1.5σ, it is treated as an interface atom (Sec. S3C). The location of the liquid–vapor interface is then defined as the average z-position of the interface atoms.

Because an accurate P_d is essential, we calculated it using two independent approaches. The first approach is to directly apply Eq. (2). In the EMD systems with a solid component, film thicknesses between 0.6 and 6 nm were studied with temperatures between 85 and 100 K. For each configuration, the pressure in the vapor phase is obtained after the system reaches thermal equilibrium. This pressure is $P_{eq}(T_{lv})$. P_d is then calculated from Eq. (2) with $P_{sat}(T_{lv})$ and $\rho_l(T_{lv})$ from the EMD system where no solid is present and $P_c = 0$. The resulting P_d values (based on the average of three simulations differentiated by their initial velocity distribution) are plotted in Fig. 3 vs the film thickness. Yu and Wang reported a film thickness of 1.2 nm where the P_d of an LJ argon fluid starts to increase dramatically,[31] which agrees with our results.

The second approach is by calculating the chemical potential.[48,49] At thermal equilibrium,

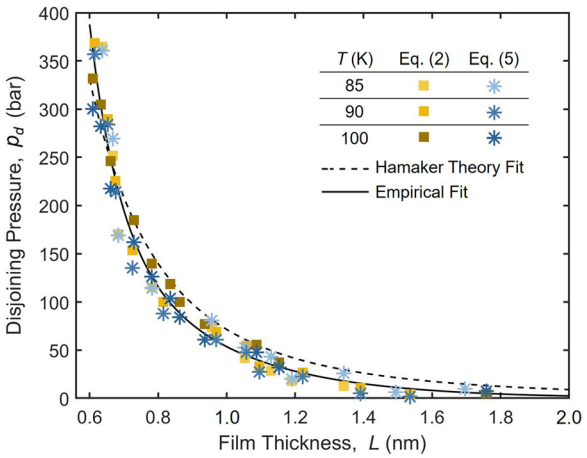

FIG. 3. Disjoining pressure vs film thickness. The dashed and solid curves represent different fitting equations obtained using all available data. The Hamaker theory fit is $1.35 \times 10^3/(6\pi L^3)$ (bar). The empirical fit is $2.63 \times 10^5 \exp(-11.9L) + 1.16 \times 10^3 \exp(-3.11L)$ (bar).

$$P_d = P_{thin} - P_{bulk} + \rho_{l,bulk}(\mu_{l,bulk} - \mu_{l,thin}), \tag{5}$$

where P_{thin} is the normal pressure of the thin film, P_{bulk} is the normal pressure in a film thick enough that the equilibrium vapor pressure equals the saturation vapor pressure (i.e., where $P_d = 0$), $\rho_{l,bulk}$ is the density of the bulk liquid, and $\mu_{l,bulk}$ and $\mu_{l,thin}$ are the chemical potentials of the bulk liquid and thin film. The chemical potentials are calculated using the Widom insertion method,[50] which is described in Sec. S3D. The bulk film properties are averaged from eleven simulations of different film thicknesses between 6 and 14 nm. For each film thickness in Fig. 3, the simulations are differentiated by their initial velocity distribution. The P_d values plotted in Fig. 3 correspond to an average over three simulations.

The values of P_d calculated from the two approaches agree well. The largest relative error of 10% is at the smallest film thickness of 0.6 nm at a temperature of 100 K. Such good agreement is consistent with a previous study.[32] We do not observe any temperature dependence on P_d in this study. Bhatt *et al.*[48] found an increase in P_d with decreasing film thickness and increasing temperature. We note that they worked on an LJ system with two vapor media interacting across a liquid layer with thicknesses between 1.6 and 2.1 nm at temperatures of 103 and 109 K, which does not overlap with our data.

Classic Hamaker theory predicts that $P_d = A/(6\pi L^3)$.[51] For a non-polar material, A can be calculated from

$$A = \pi^2(n_s n_v C_{sv} + n_l n_l C_{ll} - n_l n_s C_{sl} - n_l n_v C_{lv}), \tag{6}$$

where the subscript s refers to the solid phase, n is the number density, and $C = 4\varepsilon\sigma^6$. The absolute values of A calculated from Eq. (6) at temperatures of 85, 90, and 100 K are 1.27×10^3, 1.24×10^3, and 1.19×10^3 bar-nm^3. These values are comparable to the A fit to all data of $(1.35 \pm 0.06) \times 10^3$ bar-nm^3. Plotting the classic Hamaker theory (dashed line in Fig. 3) results in a root mean square error (RMSE) of 27 bar. We note that classic Hamaker theory has approximations that may not be satisfied in ultra-thin films.[32] These include (i) the continuum assumption, which may break down, and (ii) ignoring the repulsive part of the interatomic potential. To obtain an empirical relation between P_d and L for use in Eq. (1), we chose to fit the simulation data with the sum of two exponential terms (solid line in Fig. 3), leading to a 20% smaller RMSE than that from classic Hamaker theory.

We also checked if α is influenced by P_d. As shown in Fig. S2(b), all but one of the α values calculated for thin films are in the range reported in the literature for bulk liquid films. For the one outlier, it is within 1% of the closest literature value. Thus, α is not influenced by P_d and the values for a bulk film can be used.

The predicted $\dot{m}''_{evap}$ values are plotted in Fig. 4 and its inset as a function of film thickness. The black line is determined directly from NEMD. The gold squares are the HKS predictions including P_d and

the blue stars are the HKS predictions with $P_d = 0$ (i.e., $P_{eq} = P_{sat}$). All three predicted $\dot{m}''_{evap}$ increase with decreasing thickness until a thickness of around 1.5 nm is reached. The increase is a result of the decreasing liquid conduction resistance, which leads to a higher T_{lv}. When the film thickness is smaller than 1.5 nm, the direct simulation $\dot{m}''_{evap}$ decreases dramatically. It is at this thickness that P_d becomes important, which is consistent with the transition length scale in Fig. 3. The interactions between the solid and liquid atoms prevent the liquid atoms from evaporating, even with an increased superheat. When the film thickness decreases to 0.6 nm (around 2 layers of liquid atoms), the direct NEMD $\dot{m}''_{evap}$ reaches zero and no longer changes. This thickness corresponds to the adsorbed film thickness [region (i) in Fig. 1].

The direct NEMD $\dot{m}''_{evap}$ and the theoretical HKS $\dot{m}''_{evap}$ calculated with P_d show good agreement with an RMSE of 10% (77 kg/m^2-s) based on the bulk film value. This result is a clear demonstration of the validity of the HKS theory when P_d is non-negligible.

When the film thickness is larger than 1.5 nm, the HKS predictions with and without P_d are indistinguishable. When the film thickness decreases below 1.5 nm, however, not including P_d leads to an increasing $\dot{m}''_{evap}$, which is incorrect. Different reservoir temperatures were created to test the robustness of our conclusion (Sec. S4). The direct NEMD $\dot{m}''_{evap}$ also agrees well with the theoretical HKS $\dot{m}''_{evap}$ for driving reservoir temperature differences of 10 K (RMSE = 43 kg/m^2-s) and 20 K (RMSE = 96 kg/m^2-s). In all cases, P_d becomes important when the film thickness is below 1.5 nm.

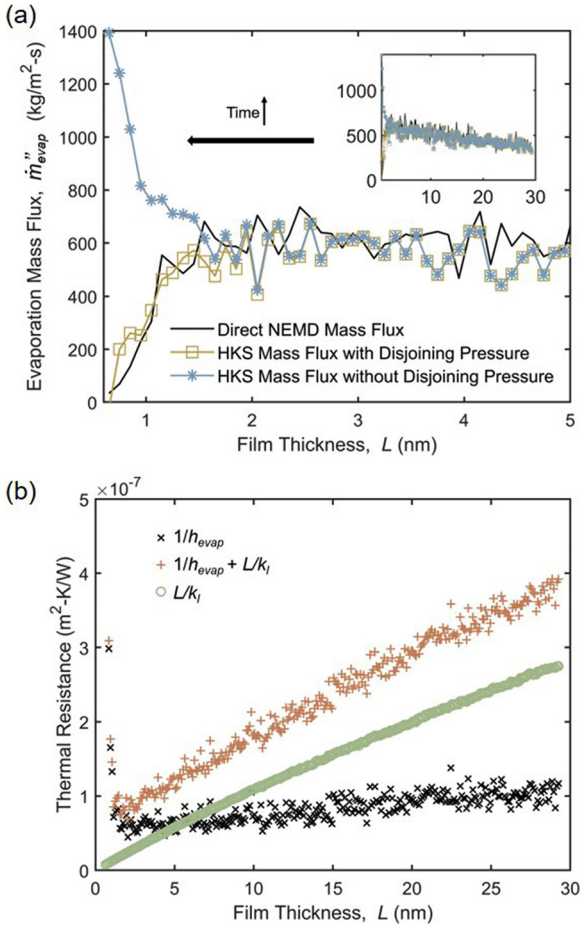

FIG. 4. (a) Evaporation mass flux vs film thickness at small film thicknesses when the reservoir temperature difference is 30 K. The inset shows the whole profile. Lines are given as guides to the eye. (b) The thickness dependence of the evaporation resistance and liquid conduction resistance.

We now consider the role of the liquid conduction and evaporation thermal resistances in the evaporation. The evaporation resistance is $1/h_{evap}$, where h_{evap} is the evaporation heat transfer coefficient calculated from $\dot{m}''_{evap}h_{fg}/(T_{lv} - T_v)$ and h_{fg} is the latent heat, which is calculated as described in Sec. S5.[52] We obtain an average h_{evap} of 1.25×10^7 W/m^2-K in the bulk film region for the 30 K reservoir temperature difference. The liquid conduction resistance is L/k_l, where k_l is the thermal conductivity of liquid LJ argon obtained from Ref. 53. The thickness-dependent resistances and their sum are plotted in Fig. 4(b). To estimate the point where the two individual resistances are equal, we define the evaporation Kapitza length as $L_{K,evap} = k_l/h_{evap}$. The evaporation Kapitza length corresponds to the liquid film thickness that has the same thermal resistance as that set by the evaporation heat transfer coefficient. For our system, with an average k_l of 0.1 W/m-K and the average h_{evap} from above, $L_{K,evap}$ is found to be 8 nm, close to where the liquid conduction and evaporation resistances equate in Fig. 4(b). From a design perspective, the total thermal resistance should be minimized so as to maximize the evaporation rate. From Fig. 4(b), we see that the liquid conduction resistance dominates for film thicknesses greater than $L_{K,evap}$. This result suggests that micro/nano-scale surface structures that force the liquid film thickness to be comparable to or smaller than $L_{K,evap}$, but larger than the adsorbed film thickness, will maximize the evaporation rate. We further propose $L_{K,evap}$ as the film thickness for distinguishing regions (ii) and (iii) in the meniscus (Fig. 1), as that is the thickness beyond which the liquid conduction resistance dominates the total resistance.

For other fluid–solid combinations and system parameters, the evaporation mass flux and the associated meniscus length scales will change. For example, an increased fluid-solid interaction strength will lead to (i) more layering of the liquid atoms on the solid,[54] which will decrease the solid–liquid interfacial thermal resistance[55] and, in turn, decrease the liquid–vapor interfacial temperature, resulting in an increased evaporation mass flux and (ii) an increased disjoining pressure, which will decrease the evaporation mass flux in the thin film region. While such systems are interesting and important, we do not believe that their exploration will change our conclusions.

In summary, we applied MD simulations to demonstrate the validity of the HKS relation for predicting the evaporation mass flux in the presence of disjoining pressure. This validation indicates that the HKS relation can be applied to analyze micro heat pipes and miniature thermosyphons, where the disjoining pressure is significant. We also analyzed the system thermal resistances and determined that surface structures that make the liquid film thickness comparable to or smaller than the evaporation Kapitza length are essential for maximizing the evaporation mass flux. Our results set the stage for future studies on more complicated fluids.

See the supplemental material for the details of the NEMD and EMD simulations and results for different driving temperature differences.

This work was supported by the NSF ENG Directorate, CBET Division, Award No. 1804752.

DATA AVAILABILITY

The data that support the findings of this study are available from the corresponding author upon reasonable request.

REFERENCES

[1]E. Pop, "Energy dissipation and transport in nanoscale devices," Nano Res. **3**, 147–169 (2010).
[2]A. Majumdar, "Helping chips to keep their cool," Nat. Nanotechnol. **4**, 214–215 (2009).
[3]J. A. Weibel, S. V. Garimella, and M. T. North, "Characterization of evaporation and boiling from sintered powder wicks fed by capillary action," Int. J. Heat Mass Transfer **53**, 4204–4215 (2010).
[4]Y. Nam, S. Sharratt, C. Byon, S. J. Kim, and Y. S. Ju, "Fabrication and characterization of the capillary performance of superhydrophilic Cu micropost arrays," J. Microelectromech. Syst. **19**, 581–588 (2010).
[5]S. M. Sajadi, N. Farokhnia, P. Irajizad, M. Hasnain, and H. Ghasemi, "Flexible artificially-networked structure for ambient/high pressure solar steam generation," J. Mater. Chem. A **4**, 4700–4705 (2016).
[6]H. Ma and G. Peterson, "Temperature variation and heat transfer in triangular grooves with an evaporating film," J. Thermophys. Heat Transfer **11**, 90–97 (1997).
[7]N. Farokhnia, P. Irajizad, S. M. Sajadi, and H. Ghasemi, "Rational micro/nanostructuring for thin-film evaporation," J. Phys. Chem. C **120**, 8742–8750 (2016).
[8]A. H. Elsheikh, S. W. Sharshir, M. K. A. Ali, J. Shaibo, E. M. Edreis, T. Abdelhamid, C. Du, and Z. Haiou, "Thin film technology for solar steam generation: A new dawn," Sol. Energy **177**, 561–575 (2019).
[9]X. Luo, C. Huang, S. Liu, and J. Zhong, "High performance of carbon-particle/bulk-wood bi-layer system for solar steam generation," Int. J. Energy Res. **42**, 4830–4839 (2018).
[10]E. Cvitkovic, E. Klaus, and F. Lockwood, "A thin-film test for measurement of the oxidation and evaporation of ester-type lubricants," ASLE Trans. **22**, 395–401 (1979).
[11]K. D. Danov, N. Alleborn, H. Raszillier, and F. Durst, "The stability of evaporating thin liquid films in the presence of surfactant. I. Lubrication approximation and linear analysis," Phys. Fluids **10**, 131–143 (1998).
[12]H. Tuo and P. Hrnjak, "Visualization and measurement of periodic reverse flow and boiling fluctuations in a microchannel evaporator of an air-conditioning system," Int. J. Heat Mass Transfer **71**, 639–652 (2014).
[13]M. Shannon, T. Leicht, P. S. Hrnjak, N. Miller, and F. Khan, "Thin-film resistance sensor for measuring liquid mass fraction in super-heated refrigerant," Sens. Actuators, A **88**, 164–177 (2001).
[14]R. J. Klimchak and P. G. Glavinos, Jr., "Manufacture of liposomes and lipid-protein complexes by ethanolic injection and thin film evaporation," U.S. patent 6,120,795 (2000).
[15]D. E. Ott, "Desertification of the peritoneum by thin-film evaporation during laparoscopy," J. Soc. Laparoendosc. Surg. **7**, 189 (2003).
[16]B. Derjaguin, S. Nerpin, and N. Churaev, "Effect of film transfer upon evaporation of liquids from capillaries," RILEM Bull. **29**, 93–98 (1965).
[17]H. Hu, J. A. Weibel, and S. V. Garimella, "Role of nanoscale roughness in the heat transfer characteristics of thin film evaporation," Int. J. Heat Mass Transfer **150**, 119306 (2020).
[18]M. Potash, Jr. and P. Wayner, Jr., "Evaporation from a two-dimensional extended meniscus," Int. J. Heat Mass Transfer **15**, 1851–1863 (1972).
[19]P. Wayner, Jr., Y. Kao, and L. LaCroix, "The interline heat-transfer coefficient of an evaporating wetting film," Int. J. Heat Mass Transfer **19**, 487–492 (1976).
[20]F. Renk and P. Wayner, "An evaporating ethanol meniscus—Part I: Experimental studies," J. Heat Transfer **101**, 55–58 (1979).
[21]F. Renk and P. Wayner, Jr., "An evaporating ethanol meniscus—Part II: Analytical studies," J. Heat Transfer **101**(1), 59–62 (1979).
[22]K. Park, K.-J. Noh, and K.-S. Lee, "Transport phenomena in the thin-film region of a micro-channel," Int. J. Heat Mass Transfer **46**, 2381–2388 (2003).
[23]H. Wang, S. V. Garimella, and J. Y. Murthy, "Characteristics of an evaporating thin film in a microchannel," Int. J. Heat Mass Transfer **50**, 3933–3942 (2007).
[24]M. Knudsen and J. Partington, "The kinetic theory of gases; some modern aspects," J. Phys. Chem. **39**, 307–307 (1935).
[25]R. W. Schrage, *A Theoretical Study of Interphase Mass Transfer* (Columbia University Press, 1953).
[26]G. Barnes, "The effects of monolayers on the evaporation of liquids," Adv. Colloid Interface Sci. **25**, 89–200 (1986).
[27]G. Fang and C. Ward, "Temperature measured close to the interface of an evaporating liquid," Phys. Rev. E **59**, 417 (1999).
[28]C. Ward and D. Stanga, "Interfacial conditions during evaporation or condensation of water," Phys. Rev. E **64**, 051509 (2001).
[29]R. Marek and J. Straub, "Analysis of the evaporation coefficient and the condensation coefficient of water," Int. J. Heat Mass Transfer **44**, 39–53 (2001).
[30]Z. Liang, T. Biben, and P. Keblinski, "Molecular simulation of steady-state evaporation and condensation: Validity of the Schrage relationships," Int. J. Heat Mass Transfer **114**, 105–114 (2017).
[31]J. Yu and H. Wang, "A molecular dynamics investigation on evaporation of thin liquid films," Int. J. Heat Mass Transfer **55**, 1218–1225 (2012).
[32]M. Han, "Evaporation and disjoining pressure of ultrathin film on substrate: A molecular dynamics study," J. Mech. Sci. Technol. **26**, 2275–2284 (2012).
[33]Z. Liang and P. Keblinski, "Molecular simulation of steady-state evaporation and condensation in the presence of a non-condensable gas," J. Chem. Phys. **148**, 064708 (2018).
[34]R. Hołyst, M. Litniewski, and D. Jakubczyk, "A molecular dynamics test of the Hertz–Knudsen equation for evaporating liquids," Soft Matter **11**, 7201–7206 (2015).
[35]E. M. Yezdimer, A. A. Chialvo, and P. T. Cummings, "Examination of chain length effects on the solubility of alkanes in near-critical and supercritical aqueous solutions," J. Phys. Chem. B **105**, 841–847 (2001).
[36]G. Nagayama and P. Cheng, "Effects of interface wettability on microscale flow by molecular dynamics simulation," Int. J. Heat Mass Transfer **47**, 501–513 (2004).
[37]S. Plimpton, "Fast parallel algorithms for short-range molecular dynamics," J. Comput. Phys. **117**, 1–19 (1995).
[38]E. Landry, S. Mikkilineni, M. Paharia, and A. J. H. McGaughey, "Droplet evaporation: A molecular dynamics investigation," J. Appl. Phys. **102**, 124301 (2007).
[39]S. Sumardiono and J. Fischer, "Molecular simulations of droplet evaporation by heat transfer," Microfluid. Nanofluid. **3**, 127–140 (2007).
[40]S. Sumardiono and J. Fischer, "Molecular simulations of droplet evaporation processes: Adiabatic pressure jump evaporation," Int. J. Heat Mass Transfer **49**, 1148–1161 (2006).
[41]A. Faghri, *Heat Pipe Science and Technology* (Global Digital Press, 1995).
[42]D. A. McQuarrie and J. D. Simon, *Molecular Thermodynamics* (University Science Books, Sausalito, 1999).
[43]Y. A. Çengel, R. H. Turner, and J. M. Cimbala, *Fundamentals of Thermal-Fluid Sciences* (McGraw-Hill, New York, 2001), Vol. 703.
[44]Y. V. C. Rao, *Chemical Engineering Thermodynamics* (Universities Press, 1997).
[45]T. Ishiyama, T. Yano, and S. Fujikawa, "Molecular dynamics study of kinetic boundary condition at an interface between argon vapor and its condensed phase," Phys. Fluids **16**, 2899–2906 (2004).
[46]T. Ishiyama, T. Yano, and S. Fujikawa, "Kinetic boundary condition at a vapor–liquid interface," Phys. Rev. Lett. **95**, 084504 (2005).
[47]P. R. ten Wolde and D. Frenkel, "Computer simulation study of gas–liquid nucleation in a Lennard-Jones system," J. Chem. Phys. **109**, 9901–9918 (1998).
[48]D. Bhatt, J. Newman, and C. Radke, "Molecular simulation of disjoining-pressure isotherms for free liquid, Lennard-Jones thin films," J. Phys. Chem. B **106**, 6529–6537 (2002).
[49]M. Han, "Disjoining properties of Ne and Ar on graphite surface," Colloids Surf., A **317**, 679–686 (2008).
[50]D. Frenkel and B. Smit, *Understanding Molecular Simulation: From Algorithms to Applications* (Elsevier, 2001), Vol. 1.
[51]H. C. Hamaker, "The London-Van der Waals attraction between spherical particles," Physica **4**, 1058–1072 (1937).
[52]J. Wang and T. Hou, "Application of molecular dynamics simulations in molecular property prediction. 1. Density and heat of vaporization," J. Chem. Theory Comput. **7**, 2151–2165 (2011).
[53]A. J. H. McGaughey and M. Kaviany, "Phonon transport in molecular dynamics simulations: Formulation and thermal conductivity prediction," Adv. Heat Transfer **39**, 169–255 (2006).
[54]J. A. Thomas, A. J. H. McGaughey, and O. Kuter-Arnebeck, "Pressure-driven water flow through carbon nanotubes: Insights from molecular dynamics simulation," Int. J. Therm. Sci. **49**, 281–289 (2010).
[55]D. Alexeev, J. Chen, J. H. Walther, K. P. Giapis, P. Angelikopoulos, and P. Koumoutsakos, "Kapitza resistance between few-layer graphene and water: Liquid layering effects," Nano Lett. **15**, 5744–5749 (2015).